**IMAV2017-35**
http://www.imavs.org/pdf/imav.2017.35



# Bond Graph based design tool for a passive rotation flapping wing

Le Anh Doan*, Christophe Delebarre, Sebastien Grondel, Eric Cattan

*Abstract*— Micro air vehicles (MAVs) are becoming more popular over larger unmanned aerial vehicles (UAVs) as they are easily portable, more discreet and less dangerous in case of a crash. Among common types of MAVs, the flapping wing configuration shows incredibly potential flying skills such as hovering, flying backward and recovering after shock. However, designer faced many difficulties due to the micro-size of the MAVs. In this work, we propose a numerical model based on Bond Graph for our flapping MAV which allows us to analyze the wing kinematic and thus predict the total lift force. This Bond Graph model employs the quasi-steady aerodynamic theory and the Lagrange dynamic equation as the main principles. A proper wing kinematic which allows the enhancement of the total lift force could be derived from this model based on the non-linear optimization of the system's sensitivity parameters such as spring stiffness, working frequency and input voltage... A prototype is fabricated and characterized. Comparing the experiment and the simulation, the model is able to predict the wing movement and the mean lift force, and therefore could be used as a design tool. A take-off demonstration is provided to confirm our results.

***Keywords*—**UAV, MAV, flapping wing, numerical model, Bond Graph.

## 1 INTRODUCTION

The performance of the existing designs of the flapping wing MAVs are worse compared to the fixed and rotary wing groups. Low Reynolds number condition leads to highly unsteady aerodynamics of such vehicles). Nevertheless, the perspective of potentially achieving the exceptional flying performances has prompted a significant amount of research on the kinematics and aerodynamics of flapping flight in nature [1], [2], [3]. Subsequently, several studies have considered how vehicle designs could mimic the function or the form of flying organisms [4], [5], [6]. Here we introduce three outstanding existing insect-like flapping MAVs including DelFly, AV Hummingbird and Robobee. The DelFly is a tail fully controllable MAV [7]. Its Micro version is currently accepted as the smallest free flying controllable flapping wing MAV equipped with a camera and a video transmitter. This 10 cm wing span vehicle weighs 3.07 grams and can fly around 3 minutes. The 16 cm span and 19 g AV Hummingbird is a tailless remote controlled NAV built to mimic a hummingbird [8]. The tailless design makes it closer to a real flying humming bird, but leads to a passively unstable attitude. As a result, it needs a more advanced control system to stabilize the vehicle. Equipped with a small video camera for the purpose of surveillance and reconnaissance, this vehicle operates in the air for up to 11 minutes at 18km/h. Inspired by the biology of a bee, the Harvard RoboBee [9] is the smallest and lightest MAV that can perform controlled hovering. This vehicle weighs less than one-tenth of a gram, and flies using "artificial muscles" composed of materials that contract when a voltage is applied.

As the first example of MAV is passively stable with tail and the last one is limited in payload, it is thus decided to develop a flapping MAV mimicking the hummingbird. The developed MAV, however, is lighter in weight compared to the AV Hummingbird. To preserve the wing kinetic energy and to achieve a capable resonant system, we directly drive our flapping wing MAV using conventional DC motors coupled with helical springs. Flexible part that is added to the wing contributes to the wing's passive rotational movement. With the presence of elastic components in the system, higher efficiency would be achieved. The concept of this flapping MAV is shown in the Figure 1. This configuration allows us to utilize some of the off-the-shelf parts as well as available technology framework.

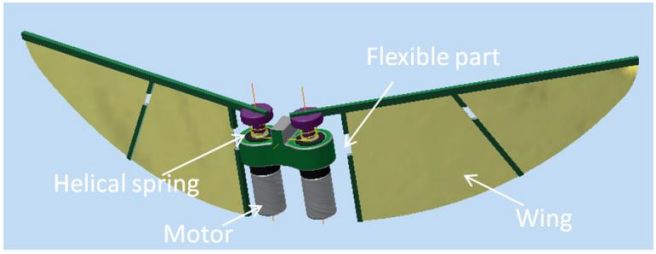


Figure 1: MAV concept

Since the studied system combines the mechanical, the electromagnetic and the aerodynamics fields, a unique model Bond Graph formalism has been set up. This kind of formalism is widely used to model multiphysics systems and energetics efficiency. Combining the Lagrange dynamic equations with a quasi-steady model of aerodynamic forces, this model serves as a tool for diagnostic system's performance. Thanks to the simulation, the MAV is able to operate at its resonant frequency with a specific torsion spring. Further optimization on the stiffness of flexible part contributes to a proper phase shift between flapping and rotational movements, which certainly results in an enhancement of total lift force. To prove the rightness of the model, a prototype is fabricated with components whose characteristics are retrieved from the simulation. The wing's motion tracked with a high-speed camera and the mean lift force measurement are used to validate the model. A take-off demonstration is also provided to confirm our results.

This article is inspired by the work of L. Hines et. al in [10] with three main different contributions. Firstly, the flexible part made by a piece of rubber is positioned along the longest chord of the wing. This helps reducing the length of the wing offset which brings the wing and also the center of

Le Anh Doan is with the University of Valenciennes, IEMN, CNRS UMR-8520, Valenciennes, France (e-mail: Leanh.Doan@etu-valenciennes.fr).

the lift closer to the actuator. This configuration also helps to vary the stiffness of the flexible part easily by modifying the rubber pieces 'dimensions. Secondly, simulation part shows the effort to approach the resonance to maximum lift forces by choosing a proper torsional spring. Lastly, to fulfill a design tool, the effect of wing offset $d_w$ and wing flexure stiffness $K_w$ on rotational amplitude, lift force and phase shift is also taken into account.

## 2 MAV MODEL

### 2.1 The Word Bond Graph of the MAV

The Word Bond Graph in Figure 2 reveals the main components of MAV dynamic model. The model is similar to the well-known block diagram, with the major difference that the "bonds" which link the elements together represent bi-directional exchange of physical power. Each bond depicts instantaneous flow of energy or power denoted by a pair of power variables called flow and effort. Flapping motion of wing is induced with a sinusoidal input voltage to each motor $v = Asin(2\pi ft)$ where $A$ is the peak-to-peak voltage, $f$ is the operating frequency. The bond next to the wave generator block would present the flow of electrical power and the power variables would be the current ($i$) and the voltage ($v$), whose product is power ($P_{in}$). Likewise, the motor output angular velocity ($\omega_l$) and the torque ($\tau_l$) are flow and effort of the corresponding power ($P_{mechanic}$). A quasi-steady model is employed to model the aerodynamic forces on our passively rotating flapping wing with the aim to predict wing motion (flapping angle $\theta$ and rotational angle $\varphi$) and lift.

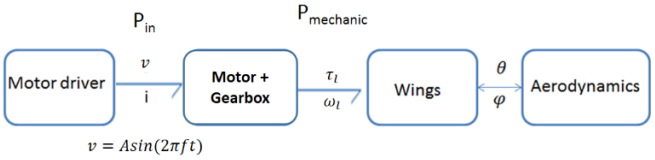


Figure 2: The Word Bond Graph of the MAV

### 2.2 Motor driver and geared motor model

While motor driver can be easily presented by a modulated effort source *MSe*, a model for a DC motor connected through a gear reduction is a little more complicated as shown in Figure 3.

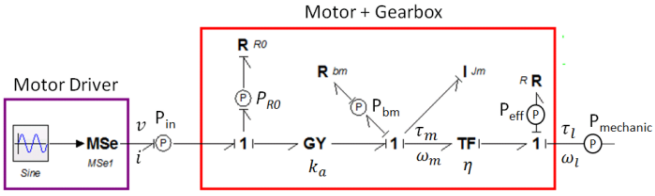


Figure 3: Motor driver and motor with gearbox blocks

The mature armature wingdings are introduced by the $R_0$ element. A gyrator GY with the armature constant, $k_a$, converts input ($v$) voltage into angular velocity ($\omega_m$). A transformer element TF stands for the gearbox with the gears ratio of $\eta$. $J_m$ and $b_m$ are the rotor inertia and motor rotational damping values respectively. The R element right next to the TF element demonstrates the gearbox efficiency. Some power sensors are integrated in the Bond Graph model to inspect input power ($P_{in}$), dissipated power ($P_{R0}$, $P_{bm}$ *and* $P_{eff}$) and the power supplied to the wing ($P_{mechanic}$).

### 2.3 Aerodynamic model

In the absence of skin friction, to model the aerodynamic forces on thin flapping wings, we employ a quasi-steady model [11], where the instantaneous aerodynamic forces on the wing are approximated using Blade Element Method. In this method, each wing is divided into a set of cross-section strips, each of width *dr*, and at a mean radius *r* from the axis of flapping. The instantaneous forces may be represented as the sum of three components, each acting normal to the wing surface:

$$F_{Lift} = F_{trans} + F_{rot} + F_{air} \quad (1)$$

where $F_{trans}$ is the translational force, $F_{rot}$ is the rotational force. The added air mass force $F_{air}$ is the inertia of the airflow generated by unsteady wing motion.

### 2.4 Wings model

The dynamic model of the wing is formulated in Lagrangian form with two coordinates of flapping ($\theta$) and rotational angle ($\varphi$).

$$L = T - V = \frac{1}{2}m_w\vec{v}.\vec{v} + \frac{1}{2}J_w\vec{\omega}.\vec{\omega} - \frac{1}{2}K_w\varphi^2 - \frac{1}{2}K_s\theta^2 \quad (2)$$

where $T$ is the total kinetic energy of the system, equalizing the sum of the kinetic energies of the wing translation and rotation, and $V$ is the potential energy of the system caused by the torsion spring and the flexible part with corresponding stiffness of $K_s$ and $K_w$. $m_w$ is the wing mass and $J_w$ is the wing inertia. The motion equations of the wing could be drawn from the derivation of the Lagrangian equations.

$$\frac{d}{dt}\left(\frac{\partial L}{\partial \dot{\varphi}}\right) - \frac{\partial L}{\partial \varphi} = \vec{M}_{aero\_rot} - b_w\dot{\varphi} \quad (3)$$

$$\frac{d}{dt}\left(\frac{\partial L}{\partial \dot{\theta}}\right) - \frac{\partial L}{\partial \theta} = \vec{M}_{drive} + \vec{M}_{aero\_flap} \quad (4)$$

where the $\vec{M}_{drive} = \tau_l$ is the driving flapping torque and also the torque provided by the motor. $b_w$ is the damping of flexible part. $\vec{M}_{aero\_rot}$ and $\vec{M}_{aero\_flap}$ are the moments due to the aerodynamic forces in the rotational and flapping direction. This approach for passive wing is inspired by the work of [10]. Reader should refer to this work for full derivation of dynamic equations.

It is noted that Equations 3 and 4 have the second order form of a spring-mass-damper system with nonlinear coefficients. They can be presented in Bond Graph by two different set of C, I, R elements for each dynamic coordinate as in Figure 4. Apart from the aerodynamic moment, the two above MSE elements also include moments caused by the gyroscopic effect and centrifugal force acted on flapping and rotational axes. Wing's Bond Graph elements can be found in Appendix To form the MAV's model, all of the sub-systems are linked together through the common bonds, presenting the power transfer as shown in Figure 5.

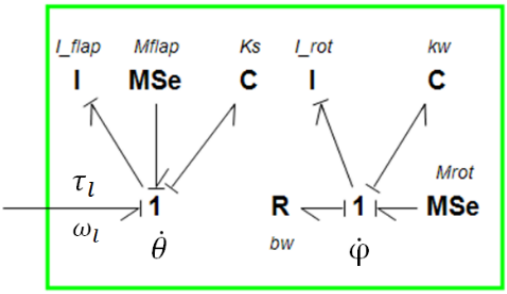


Figure 4: MAV's wing block

### 2.5 *Parameters selection*

To limit the number of free parameters, our simulated motor is based on an off-the-shelf motor (GM15A). The motor characteristics are provided by the manufacturer and also in the work of [10]. The wing geometry characteristics is retrieved from a 3D model. The added helical springs could be chosen based on the desired flapping frequency. The maximum stiffness value is also limited by the toughness of the plastic gearbox of the motor.

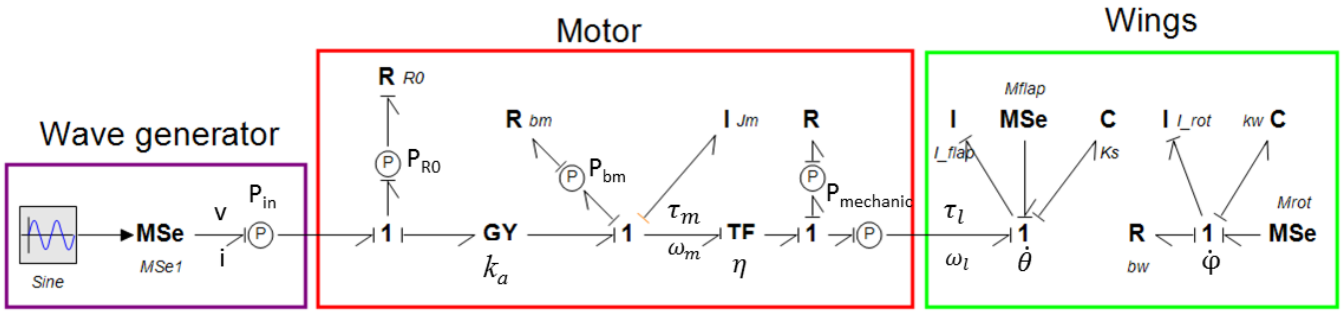


Figure 5: Bond Graph presentation of MAV

### 2.6 *Vertical take-off model*

In order for a fly vehicle to rise into air, the lift force ($F_{Lift}$) created must be at least greater than or equal to the force of gravity ($F_{Gravity}$) as shown in (5):

$$m_{MAV}\ddot{z} + f_{viscous} = F_{Lift} - F_{Gravity} \quad (5)$$

where z is the prototype's altitude and $m_{MAV}$ is the mass of prototype. Suppose that the prototype moves at relatively low speeds through the air, the viscous resistance $f_{viscous}$ is approximately proportional to its velocity:

$$f_{viscous} = -b_{vicous}\,\dot{z} \quad (6)$$

where $b_{viscous}$ is the viscous coefficient. A 1-junction is employed to present Equation 5 as in the vertical take-off block.

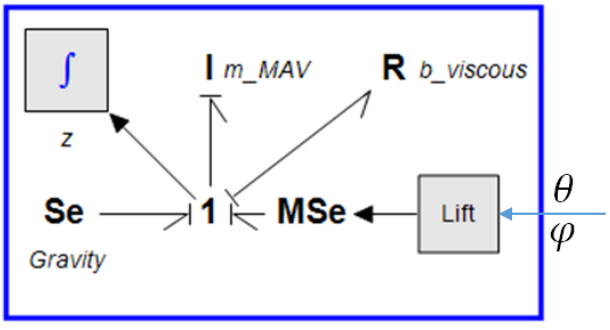


Figure 6: Vertical take-off block

## 3 SIMULATION

### 3.1 *Sensitivity to spring stiffness and driving frequency*

Three stiffness values of springs are tested on a range of input frequency from 1 to 20 Hz. The system input voltage isheld at 2V to limit the high flapping angle of the least stiff elastic element. Different colors are used to specify different elastic element stiffness systems as shown in following figures. While the system with the highest spring stiffness resonates at 8 Hz, resonance of the lowest one could not be determined. Maximum flapping amplitude of the remaining system occurs at 3 Hz.

Peak lift force, however, happens beyond the flapping resonance. At low flapping frequencies, the wing speed is too low to produce remarkable lift or wing rotation. In ascending order of stiffness, maximum mean lift occurs at 4 Hz, 7 Hz and 10 Hz respectively. It is noted that, the highest spring's stiffness brought the peak of lift close to the frequency at which the resonance happens. Performing this system at its resonance frequency allows us to optimize the system efficiency without much decreasing in lift. A compromise between wing speed and flapping angle amplitude is always the key-point to enhance the system performance.

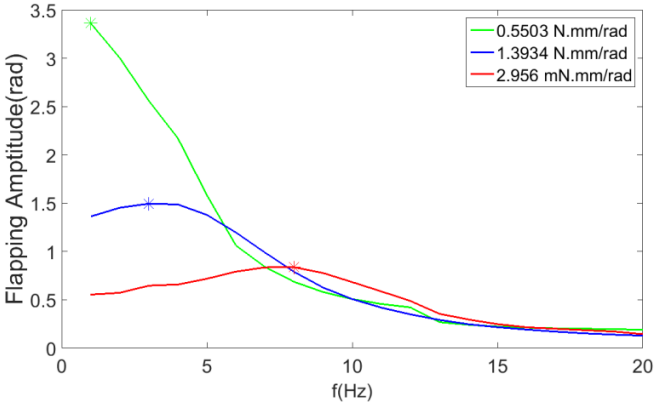


(a)

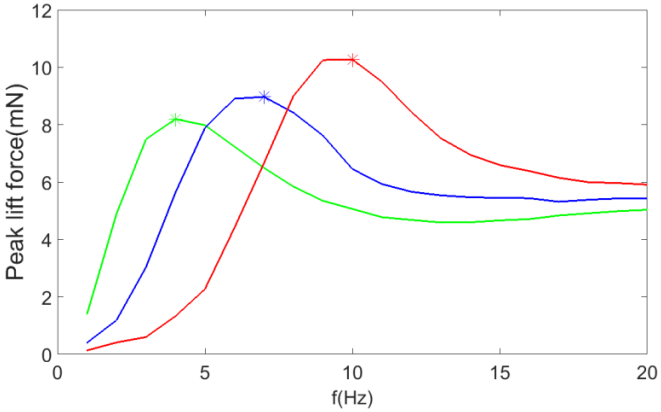


(b)

Figure 7: Effect of spring stiffness $K_s$ and flapping frequency on flapping amplitude (a) and lift force (b)

### 3.2 *Sensitivity to input voltage*

A sweep of input voltage amplitudes is simulated; the results can be seen in the next figure. Depending on the spring stiffness, the driving frequency is set to the corresponding value where the highest lift value was observed as in the previous part.

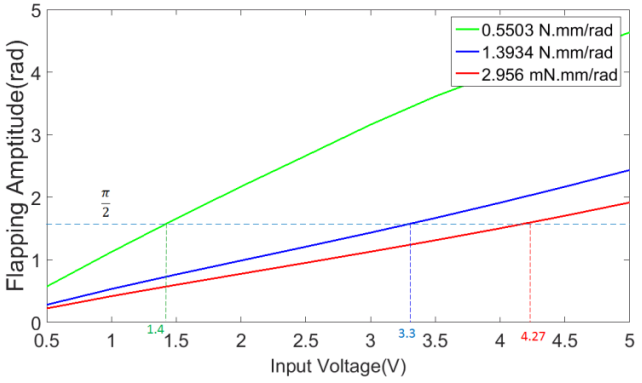


(a)

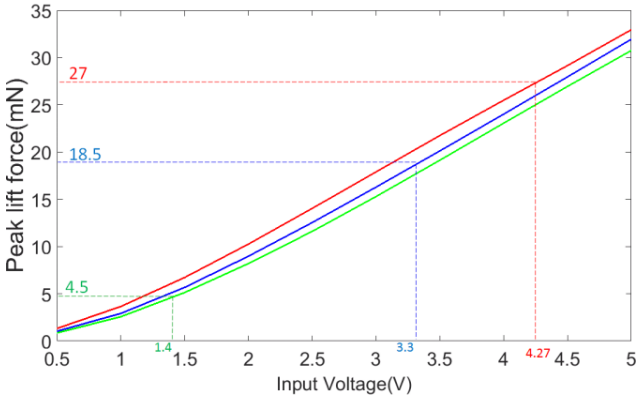


(b)

Figure 8: Effect of spring stiffness $K_s$ and input voltage on flapping amplitude (a) and lift force (b)

Figure 8(a) illustrates well a nearly linear relationship between flapping amplitude and the input voltage in the range of examination. Flapping angle is inversely proportional to the value of spring's stiffness. In reality, the flapping amplitude should not exceed pi/2 to avoid wings 'collision. With this constraint, the reachable lift forces at this flapping amplitude are 4.5 mN, 18.5 mN and 27 mN as shown in Figure 8(b). In conclusion, a system with maximum stiffness (2.956e3 mN.mm/rad) activating at 4.27 V and 10 Hz will be our ultimate solution.

### 3.3 *Sensitivity to wing flexure stiffness*

The system with spring stiffness of 2.956e3 mN.mm/rad isstimulated by an input voltage of *4.27sin(2π10t)*. Some interesting discoveries could be seen in Figure 9. It is better to remind that phase shift is the difference between rotational angle and flapping angle, a negative phase shift means the former angle is lag behind the latter and vice versa.

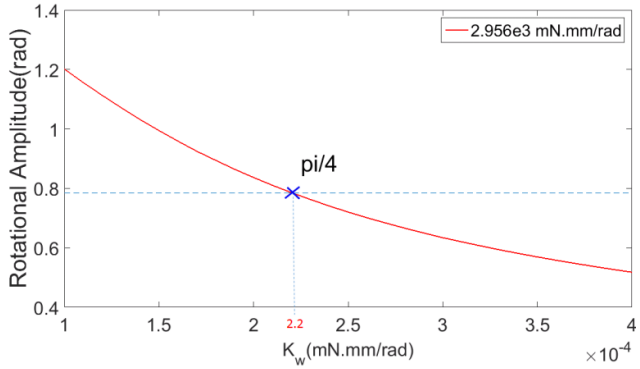


(a)

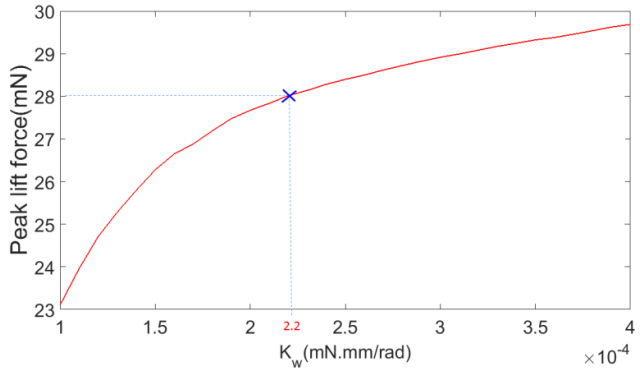


(b)

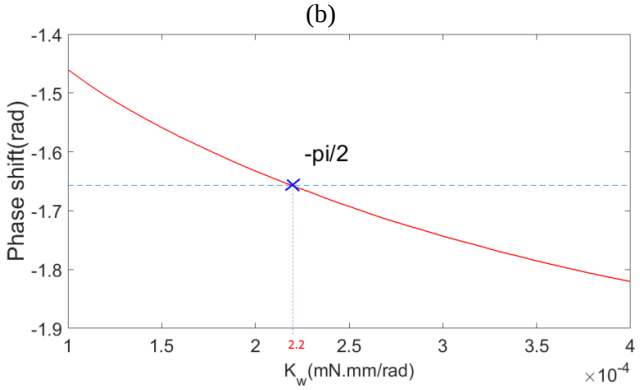


(c)

Figure 9: Effect of wing flexure stiffness $K_w$ on rotational amplitude (a) lift force (b) and phase shift (c)

It is obvious that larger value of wing flexure stiffness results in smaller rotational amplitude. A lower value than the minimum bound of inspection range (1e-4 N.m/rad) causes over rotation and the wing exhibits erratic and unsteady behavior. Lower driving frequency could generate an

acceptable wing motion, however it will not be the goal of this scope. Raising the stiffness does slowly increase the total lift force, on the other hand it also augments the angle of attack. If this angle exceeds $\pi/4$, drag coefficient will play a major role while lift coefficient gradually degrades. This means thatthe total force is less directed vertically but more horizontally.

We always expect to achieve a phase shift close to $-\pi/2$ because it leads to the highest rotational angle which occurs at midpoint of flapping trajectory where the maximum flapping velocity generates an ultimate total lift force. Fortunately, all of our desires are achieved with this configuration. This system has $\pi/4$ of rotation angle at mid-stroke and $-\pi/2$ of phase shift at a flexure stiffness of 2.2e-4 N.m/rad.

### 3.4 *Sensitivity to wing offset*

In this part, we use the same setting as the previous part except that the variable is now the wing offset.

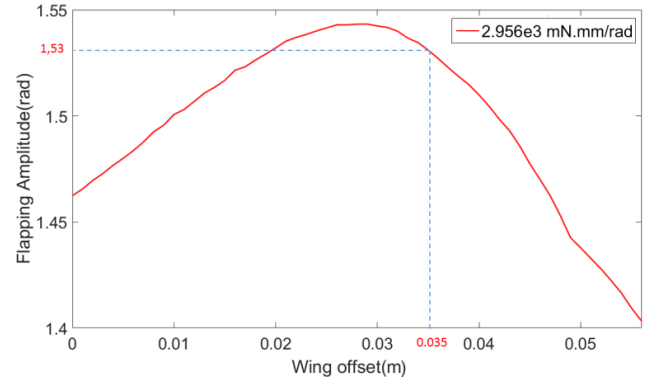


(a)

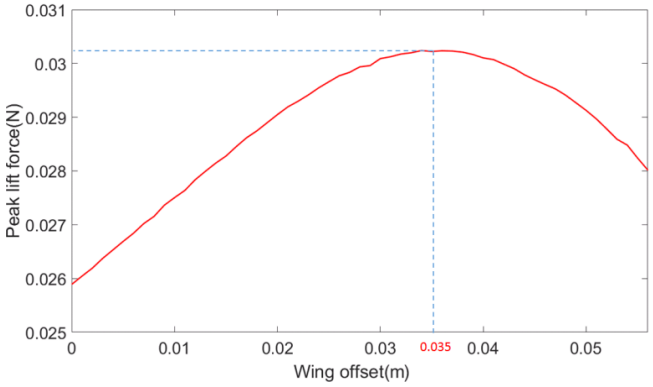


(b)

Figure 10: Effect of wing offset $d_w$ on Flapping amplitude (a) and lift force (b).

It is apparent that the wing translational velocity at the mid-chord of each wing strip is proportional to wing offset, so increasing the wing offset improves the translational force. This is well demonstrated in the range of 0 to 35 mm. However, increasing the wing offset also augments the moment inertia about the flapping axis and therefore reduces the flapping movement. While the wing size is kept constant, greater wing offset also effectively increases the damping force which can be limited given maximum motor torque. As can be seen in the Figure 10, when the wing offset is beyond 35 mm, the lift force starts to reduce. Another disadvantage of raising this parameter is that it moves the center of lift far from center gravity and makes the prototype more difficult to stabilize. Bigger size of the prototype is also another drawback. A table summarizes the optimized parameters can be found in Appendix.

### 3.5 *Dynamic simulation results*

After running the simulation with all the parameters found from previous discussions, a satisfactory wing's motion is portrayed in Figure 11. The rotation trajectory is $\pi/4$ and lags behind the flapping by nearly $\pi/2$. Notably, the force shown in Figure 11(a) is the cycle-averaged lift which is in the vertical body direction. The peak lift with the force of 17 mN occurs at each mid-stroke.

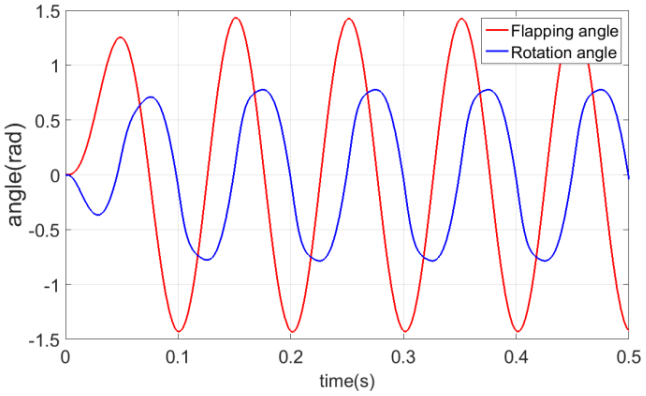


(a)

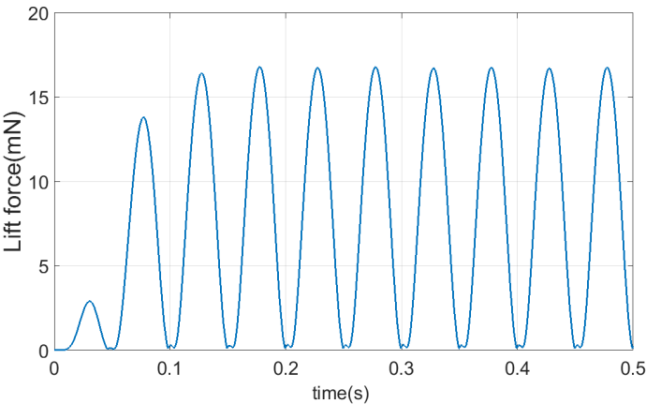


(b)

Figure 11: Dynamic simulation of a proper wing trajectory (a) and resulting lift force (b)

The results from the added vertical take-off block are illustrated in the following picture. The MAV reaches the altitude of 6 cm after 0.5 s with a 100mA peak sinusoidal input current.

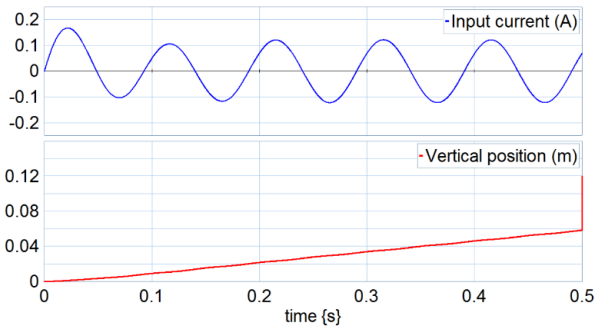


Figure 12: Simulation of vertical take-off

## 4 EXPERIMENT

After building the MAV model, we can now validate whether it reproduces the system behavior within acceptable bounds with the recommended parameters drawn from the optimization step. This section starts by the preparation of main components and materials for the MAV fabrication. Then a set of validation experiments including wings movement observation and total mean lift force estimation are conducted to confirm the rightness of our model.

### *4.1 Component fabrication*

A tiny DC pager-motor named GM15A with a planetary gearhead 25:1 reduction has been chosen as the main actuator. It is designed for a 3V nominal operation, giving 920RPM drawing 100mA. The motor is controlled by a motor driver named Pololu DRV8835. Our flapping system is induced with a Pulse Width Modulation (PWM) approximated sinusoidal voltage generated by our motor driver. The wing should be as light as possible but not flexible because it is supposed to be rigid except at the flexible part and near the rotational axis.

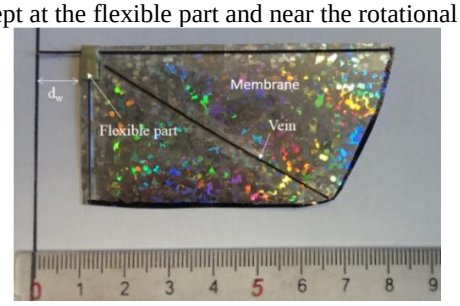


Figure 13: Fabricated Wing

The wing has the length of 8.5 cm and the maximum chord length is 3.5cm. The flexible part is made by a piece of rubber and its rotational stiffness depends on its length. $d_w$ is the offset distance from the motor output shaft to the free end of leading edge. The membrane is made by very thin film with the thickness of $25\mu m$. The mass of the wing is 0.12 g measured by a microbalance Mettler Toledo.

### *4.2 Wing kinematic observation*

To observe the wing movement, a high speed camera has been positioned in front of the wing. The half prototype is activated by an input voltage of $4.5\sin(2\pi 10t)$ (V). A $\pi/4$ of rotational angle at the mid-stroke is the validation for the mathematical model

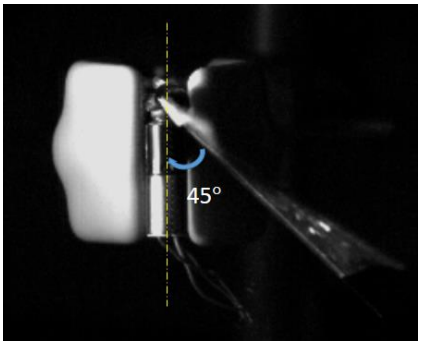


Figure 14: Diagram of wing observation experiment set-up

### *4.3 Mean lift force measurement*

The wings with the appropriate kinematic were employed in the lift force measurement experiment. The whole set-up could be seen in the Figure 15.

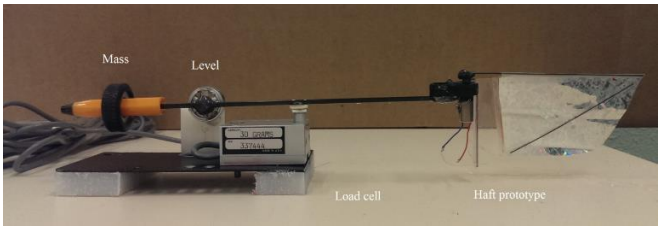


Figure 15: Lift measurement set-up

The moment created by the weight of the half prototype and the "Mass" have the same value but in the reverse direction counting at the center rotation of the level so that the level is in its balance position at the beginning. As soon as we activate the motor, the lift force is generated and measured by the load cell. A mean lift force of 4.5g could be seen in the next figure.

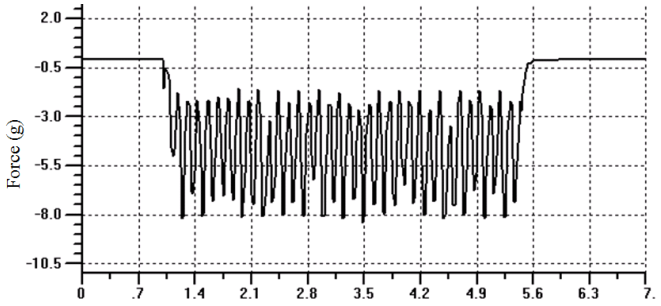


Figure 16: Force measurement

From the simple equation of equivalent moments, the lift force must be 0.4 time as much as the force measured by the load cell and therefore we get the mean value of 1.8 g. The mean lift measured from the experiment is a little bit bigger than one from the simulation, however it is still good to predict the total lift. Remind that the total mass of full prototype is 2.8 g, so it should fly if we employed two motors.

### *4.4 Take-off demonstration*

A complete prototype was assembled with recommended configuration. It was let to move up and down unrestrictedly along two fixed parallel carbon tubes which, by the way, limit all other MAV's degree of freedom. At an input voltage of 4V peak-to-peak, the system starts to fly up. After a few seconds, a snapshot of the MAV motion (Figure 17) was taken, showing that it was above the initial position nearly 2 cm. It is not correlated to the take-off simulation due to the friction of the MAV with two carbon tubes.

## 5 CONCLUSION

In this study, a design tool based on a dynamic numerical model has been proposed to analyze the wing kinematic of a new MAV and thus predict the total lift force. An elastic element placed in parallel to the gearbox output shaft and wing allows operation at resonance. The effect of varying wing offset, elastic element stiffness, and elastic wing stiffness

have been simulated in order to determine the best configuration.

After experiments, we can conclude that an adequate amount of lift force is produced to bring our prototype to the air, which validates the results of our design tool. As the lift weight ratio is equal 1.28, it is not possible to handle electrical circuits including microcontroller, motor driver, Bluetooth device and also battery at this time. Future work has to be developed on increasing the working frequency but maintaining the same wing kinematic. If we succeed to double the working frequency the lift force will increase by the factor of four and the MAV has more spare weights.

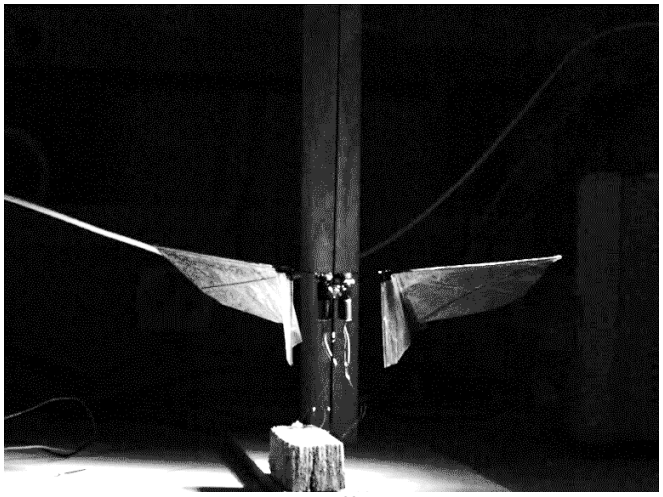

Figure 17: Take-off demonstration

## APPENDIX

As Bond Graph model of the wing shown in this work is adapted from dynamic equations in [10], readers should refer to this reference for the full derivations. The following equation introduces only the complex Bond Graph elements related to the wing.

$$I_{flap} = \sin^2(\varphi)J_{22} + \cos^2(\varphi)J_{33} + \left((R_{CG} + d_w)^2 + \frac{\beta_{CG}^2}{2}\right)m_w - \frac{1}{2}\beta_{CG}^2\cos(2\varphi)\,m_w + \eta^2 J_m \quad (7)$$

$$I_{rot} = m_w\beta_{CG}^2 + J_{11} \quad (8)$$

$$M_{rot} = \ddot{\theta}(m_w(R_{CG} + d_w)\beta_{CG}\cos(\varphi) + J_{13}\cos(\varphi)) - \dot{\theta}^2\cos(\varphi)\sin(\varphi)\,(m_w\beta_{CG}^2 + J_{22} - J_{33}) - \vec{M}_{aero}.\vec{E}_1'' \quad (9)$$

$$M_{flap} = \ddot{\varphi}\cos(\varphi)\,(m_w(R_{CG} + d_w)\beta_{CG} + J_{13}) - \dot{\varphi}^2\sin(\varphi)\,(m_w(R_{CG} + d_w)\beta_{CG} + J_{13}) + \dot{\varphi}\dot{\theta}\sin(2\varphi)\,(m_w\beta_{CG}^2 + J_{22} - J_{33}) - \vec{M}_{aero}.\vec{E}_3 \quad (10)$$

| Parameter | Value | Unit |
|---|---|---|
| $K_s$ | 2.956e3 | mN.mm/rad |
| $A$ | 3.7 | V |
| $f$ | 10 | Hz |
| $K_w$ | 220 | mN.mm.rad |
| $d_w$ | 35 | mm |
| $b_w$ | 1.5 | mN.mm.s/rad |
| $\varphi_{amplitude}$ | $\pi\backslash 4$ | rad |
| $\theta_{amplitude}$ | 1.5 | rad |
| $\phi_{lag}$ | $\pi\backslash 2$ | rad |
| $F_{peak}$ | 0.03 | N |

Table 1: Optimized parameter

## ACKNOWLEDGMENT

This work was realized within the ANR CLEAR-Flight project 13-0012-001 (Controlled lift for efficient flight of an Artificial Insect) which is supported by the French program ANR ASTRID.

## REFERENCES

[1] J. Song, H. Luo, and T. L. Hedrick, "Three-dimensional flow and lift characteristics of a hovering ruby-throated hummingbird," *Journal of The Royal Society Interface*, vol. 11, no. 98, pp. 20140541–20140541, Jul. 2014.

[2] S. P. Sane, "The aerodynamics of insect flight," *Journal of Experimental Biology*, vol. 206, no. 23, pp. 4191–4208, Dec. 2003.

[3] F.-O. Lehmann, "The mechanisms of lift enhancement in insect flight," *Naturwissenschaften*, vol. 91, no. 3, pp. 101–122, Mar. 2004.

[4] G. C. H. E. de Croon, M. Perçin, B. D. W. Remes, R. Ruijsink, and C. De Wagter, The DelFly. *Dordrecht: Springer Netherlands*, 2016.

[5] L. Ristroph and S. Childress, "Stable hovering of a jellyfish-like flying machine," *Journal of The Royal Society Interface*, vol. 11, no. 92, pp. 20130992–20130992, Jan. 2014.

[6] A. Bontemps, F. Valenciennes, S. Grondel, S. Dupont, T. Vanneste, and E. Cattan, "Modeling and evaluation of power transmission of flapping wing nano air vehicle," in *2014 IEEE/ASME 10th International Conference on Mechatronic and Embedded Systems and Applications (MESA)*, 2014, pp. 1–6.

[7] G. C. de Croon, M. A. Groen, C. De Wagter, B. Remes, R. Ruijsink, and B. W. van Oudheusden, "Design, aerodynamics and autonomy of the DelFly," Bioinspir. Biomim., vol. 7, no. 2, p. 025003, 2012.

[8] M. Keennon, K. Klingebiel, and H. Won, "Development of the Nano Hummingbird: A Tailless Flapping Wing Micro Air Vehicle," 2012.

[9] K. Y. Ma, P. Chirarattananon, S. B. Fuller, and R. J. Wood, "Controlled Flight of a Biologically Inspired, Insect-Scale Robot," Science, vol. 340, no. 6132, pp. 603–607, May 2013.

[10] L. Hines, D. Campolo, and M. Sitti, "Liftoff of a motor-driven, flapping-wing microaerial vehicle capable of resonance," *Robotics, IEEE Transactions* on, vol. 30, no. 1, pp. 220–232, 2014.

[11] W. B. Dickson, A. D. Straw, C. Poelma, and M. H. Dickinson, "An integrative model of insect flight control," in *Proceedings of the 44th AIAA Aerospace Sciences Meeting and Exhibit*, 2006, pp. 31–38.